JATIS Journal of Astronomical Telescopes, Instruments, and Systems

RESEARCH PAPER

Characterization of a proportional-integral-derivative feedback-controlled array of transition-edge sensor-bolometers in a far-infrared double-Fourier interferometry testbed

Chris S. Benson,[a,b,*] Jeremy P. Scott,[a] Locke D. Spencer,[a] Rashmi V. Sudiwala,[b,c] James Cox,[c] Tyrone Jones,[c] Berke V. Ricketti,[a,d] and Ken Wood[c]
[a]University of Lethbridge, Institute for Space Imaging Science, Lethbridge, Alberta, Canada
[b]Cardiff University, School of Physics and Astronomy, Cardiff, United Kingdom
[c]QMC Instruments, Cardiff, United Kingdom
[d]Disruptive Space Technology Centre, RAL Space, STFC-Rutherford Appleton Laboratory, Didcot, United Kingdom

ABSTRACT. Double-Fourier interferometry (DFI) from a space-based platform provides a path to achieve broadband imaging spectroscopy in the far infrared with sub-arcsecond angular resolution. To provide further study of the technique and improve its technology readiness, we have constructed a laboratory-based DFI testbed. This instrument is coupled to a custom array of 25 feedback-controlled transition-edge sensor (TES) bolometers. We present the results of characterization experiments to optimize the detector system for laboratory-based experiments involving the DFI testbed. We demonstrate that tuning the proportional-integral-derivative (PID) feedback control loops of the detectors and the timing of the multiplexed measurement process can modify the detector array's noise performance and speed of response to optical modulation for this purpose. From these, we have determined a set of optimized detector settings that reduce spectral noise in the spatial-spectral interferometer by 37% to 75%. In addition, we present a further thermal characterization of the detector array.

Keywords: detector arrays; far infrared; terahertz; Fourier spectroscopy; multiplexing

Paper 24148G received Sep. 20, 2024; revised Feb. 21, 2025; accepted Feb. 27, 2025; published Mar. 14, 2025.

1 Introduction

Approximately half of the total energy density of electromagnetic radiation emitted by stars and accreting objects in the universe throughout cosmic time, with the exception of the sun, is observed in the far-infrared (far-IR) regime (loosely defined as encompassing ∼30 to 1000 μm or 10 to 0.3 THz).[1,2] Because much of this spectral regime is largely inaccessible to ground-based observatories, the angular resolution of observations in the far-IR lags behind what has become readily available at other wavelengths ranging from radio to X-ray. The development of a far-IR double-Fourier interferometer (DFI) from a space-based platform has been identified by the astronomical community as having substantial potential to open up the far-IR to sub-arcsec imaging spectroscopy and has led to several mission proposals.[3–10]

---

*Address all correspondence to Chris S. Benson, BensonC@cardiff.ac.uk

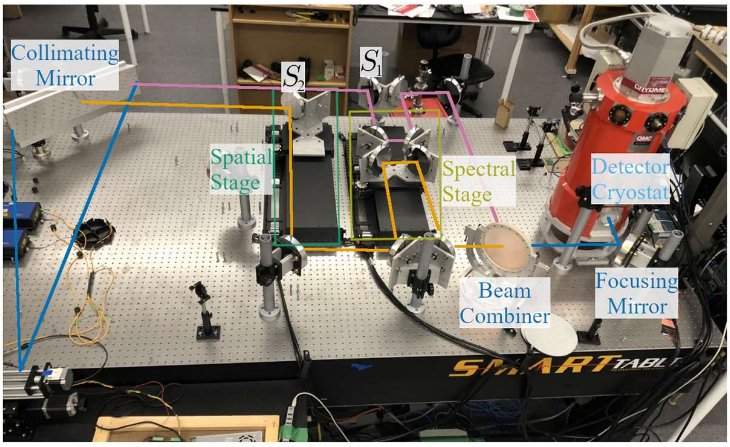

Fig. 1 Photograph of the DFI testbed and the associated detector array on the optical bench.

To progress toward a future far-IR DFI from a spaced-based platform, ground-based laboratory testbeds have been developed.[11–13] Building on this heritage, we have constructed a laboratory DFI operating within a spectral band of 200 to 2200 GHz to provide further study of the double-Fourier technique and demonstrate its capabilities for wide-field imaging spectroscopy in the terahertz regime (see Fig. 1).[14,15] The DFI testbed is coupled to a unique array of feedback-controlled transition edge sensor (TES) bolometers designed to provide a versatile detector array for the development and testing of astronomical far-infrared instruments in a laboratory setting. These operate without superconducting quantum interference devices (SQUIDs) while maintaining sufficient sensitivity for use in room-temperature far-IR/THz instruments. In this paper, we present and discuss the characterization of this TES array and its optimization for use as a detector system for the DFI testbed. This investigation has led to a 37% to 75% reduction in the spectral noise of measurements made with the interferometer which has significantly reduced the time required to obtain spatial and spectral measurements with the DFI with adequate signal to noise.

1.1 TES Bolometer Theory

The voltage response of a bolometer to a change in optical load can be written[16–18]

$$S_V = \frac{I_{\text{bias}} \alpha R_{\text{TES}}(T)}{T G_e} \frac{1}{1 + i\omega_s \tau_e}, \tag{1}$$

where ω_s is the small signal oscillation in observed light, T is the temperature of the detector, $R(T)$ is the electrical resistance of the thermometer, I_{bias} is the bias current to the thermometer, and τ_e is the detector's effective time constant. In Eq. (1), $\alpha = (T/R)dR/dT$ is a unitless measure of the steepness of the superconducting transition of a TES evaluated at the steady-state temperature of the detector. The parameter $G_e = G - P_{\text{TES}}\alpha/T$, where P_{TES} is the electrical power dissipated in the thermometer, used in Eq. (1) is an effective thermal conductance which accounts for electrothermal feedback.[16] For TES bolometers, $\alpha > 0$ and it is possible for G_e to reach zero resulting in thermal runaway.[16] For this reason, it has become common to operate the TES thermometer in a constant-voltage bias such that its Joule heating decreases as its temperature (and thereby its resistance) increases under an optical load.[17,18] When operating under a constant-voltage bias, changes in the current through the TES are often sensed and amplified using a SQUID.[3,16,18] This said, examples of constant-current biased TES bolometers can be found in early developments of TES bolometers and constant-current biased TES's have seen some success using re-entrant superconductors and external feedback mechanisms.[19–21]

1.2 Feedback-Controlled TES Bolometers

The 5×5 TES detector array that is coupled to the DFI instrument is a custom system developed by QMC instruments (Cardiff, Wales) and operates with detectors in an approximately constant-current biased state, contrary to the usual constant-voltage biased operation. These detectors do not employ electrothermal feedback to maintain the operation of the bolometers about the superconducting transition of the thermometer. Instead, detectors in the QMC TES array make use of an actively controlled heating element and a proportional-integral-derivative (PID) feedback loop to maintain the thermal operating point of the detector within a carefully timed multiplexing loop. The operation of the detectors is read out and maintained by a national instruments field programmable gate array (FPGA) that multiplexes four simultaneous channels (A to D) switching through seven rows in time (0 to 6); see Fig. 2. Each detector is composed of a niobium TES thermometer, a gold heating element, and a 5-nm-thick gold absorber.

Thermal and electrical diagrams of a single detector in the array are shown in Fig. 3. Operation about the set temperature on the superconducting transition of the TES is achieved by balancing the thermal conduction to the surrounding environment of the cryostat, the optical loading on the detector, the Joule heating from the bias circuitry of the TES, with the feedback-controlled heating element. Under an increase in incident optical power, there is a change in the TES temperature state that is measured by the voltage across the TES ($\mathbf{V}_{\mathrm{TES}}$). In response, the PID feedback loop calculates the necessary reduction in heater power to maintain the setpoint at the specified time within the multiplexing cycle. In this way, the heater power provides a measure reciprocal to the optical loading on the TES detector. The steady-state power balance of a detector follows that of a typical bolometer with the addition of the heater power

$$C_a \frac{dT}{dt} = P_{\mathrm{elec}} + P_{\mathrm{opt}} + P_{\mathrm{heat}} - P_{\mathrm{bath}}\ [\mathrm{W}], \tag{2}$$

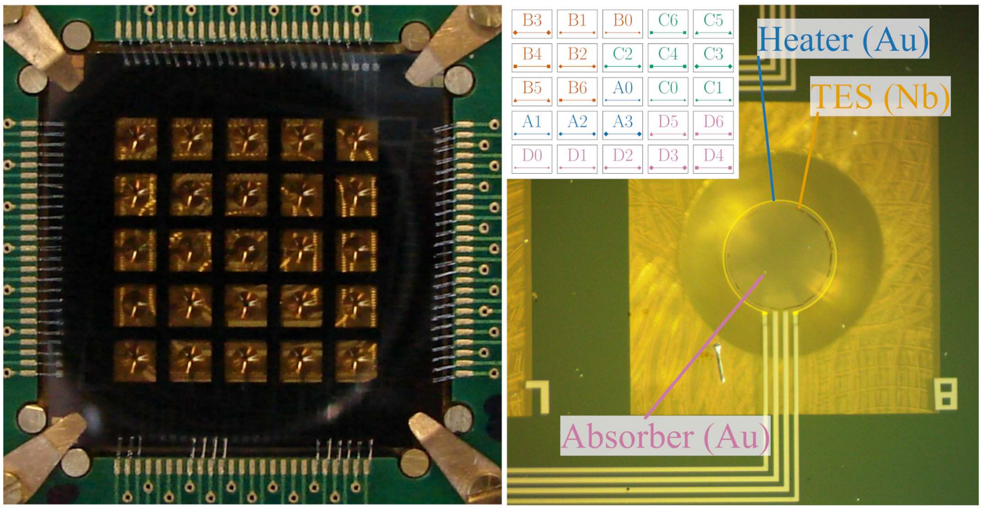

Fig. 2 Left panel shows a photograph of the array of TES detectors. The right panel shows a photograph of a single detector in the array. The circular heater and TES thermometer are marked. The order in which detectors are multiplexed by the FPGA readout system is outlined in the inset panel.

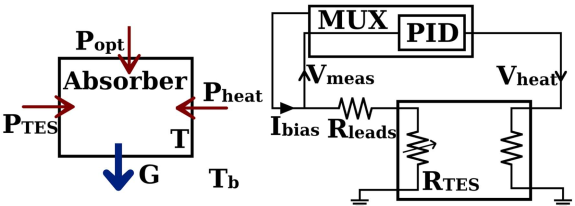

Fig. 3 Simplified thermal (left) and electrical (right) diagram of a single feedback-controlled TES bolometer in the array. The multiplexing (MUX), PID control, and detector bias are achieved through a combination of warm electronics and an FPGA.

where C_a is the lumped heat capacity of the detector and each P-term is the power provided or dissipated by the electrical bias to the thermometer, the optical loading on the detector, the heating element, and thermal conduction to the cryogenic environment. In addition, due to this operation, the response of a given detector [i.e., Eq. (1)] is modified by the transfer function of the PID controller.

This configuration allows these detectors to operate effectively under the load of a room-temperature optical system over a broadband (~200 to 2200 GHz) within a ~4 K environment (which can be easily achieved with a pulse-tube cryocooler). The detectors also make use of traditional amplifiers (Texas Instruments, INA103) rather than a SQUID-based readout, dramatically reducing the cost. In addition, this operation is highly customizable providing a versatile detector system that can be optimized for specific use cases and instruments. Despite these desirable advantages, the optically measured noise equivalent powers (NEPs) of the detectors are $\sim 5\times 10^{-12}\mathrm{W}/\sqrt{\mathrm{Hz}}$, which is not sufficiently sensitive for astronomical purposes in which detector NEPs of $\sim 5\times 10^{-16}$ $\mathrm{W}/\sqrt{\mathrm{Hz}}$ are required for background-limited observation for ground-based measurements and $\sim 5\times 10^{-20}$ $\mathrm{W}/\sqrt{\mathrm{Hz}}$ for space-based.[3,22] As the QMC TES array operates about the critical temperature of Nb (~8 to 9 K) to facilitate the advantages outlined above, it is not capable of achieving these NEPs. Instead, the detector array has been designed for the development and testing of astronomical far-IR instruments in a laboratory setting and not to compete with the sensitivities of more traditional SQUID-based TES arrays.

The detector system has been successfully commissioned and integrated into the DFI testbed and can be more fully tested within the context of the DFI.[14,15] Through the tuning of the detectors' feedback operation, the array can also be further optimized to reduce the detectors' NEPs and thereby reduce the time required to acquire high SNR spatial-spectral measurements of the DFI testbed.

1.3 Detector Operation and Adjustable Parameters

Owing to the timing of the multiplexing and feedback processes involved in a detector measurement, the detectors under study do not maintain constant operation on their superconducting transition. Instead, a detector's thermal state switches between superconducting and normal conducting states throughout a single measurement and remains within its superconducting state while other detectors in the array are measured. The result is that the time-division multiplexing (TDM) is cyclically pulsing a detector's state into operation at the desired transition region. The exact timing of the measurement process and the response of a given detector are governed by a set of user-adjustable parameters.

The adjustable parameters that modify detector behavior can be divided into two categories: parameters that adjust the timing of the multiplexing process and parameters that tune the PID control of a single detector. Detector timing parameters can be used to adjust (1) the length of a measurement pulse, (2) the duty cycle of the heater within a measurement pulse, and (3) when within a measurement pulse the TES state is measured for use in the PID feedback. A measurement pulse is divided into "loop counts" that correspond to a counter which increments when a measurement of the TES state or another operation can be completed by the FPGA. The time at which the heater switches off (having switched on at the start of a detector measurement) and the time when a TES measurement is used in PID feedback are set to occur on a given loop count. In the example shown in Fig. 4, the heater is chosen to switch off on a loop count of 4 (marked by the orange star), the TES state is measured for use in the PID on a loop count of 10 (marked by the black diamond), and the detector is inactive from loop count 11 onward (i.e., the pulse width is 11 loop counts). As these timing parameters define the TDM process, they are ubiquitous across every detector in the array. When the multiplexing cycle is turned off, the measurement cycle remains on a single row (i.e., the row counter in Fig. 4 does not increment). When in nominal operation, the sampling of the detector state is faster than the detector's effective time constant [see Eq. (1)]. It should be noted that while this assists in maintaining the PID feedback of the multiplexing cycle, these measurements do not necessarily represent statistically independent samples of a detector's thermal state. Rather, the response time of the detector to an optical signal is governed by the thermal properties of the bolometer and the multiplexed readout process (as discussed in Sec. 2).

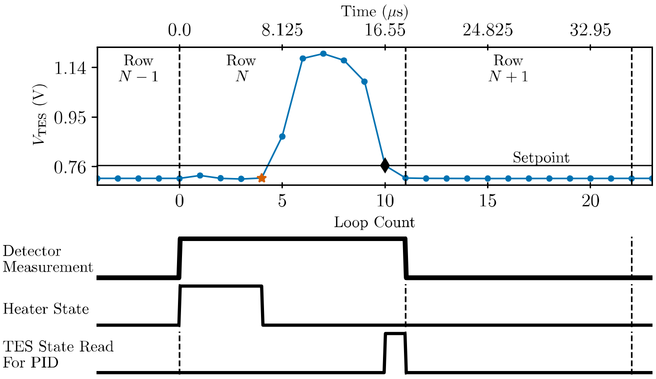

Fig. 4 Example of a single detector measurement pulse within the multiplexing cycle. When the row of the detector (N) is switched to, the TES heater becomes active for 6.5 μs at the start of the measurement pulse, the TES state is measured for use in the PID 16.25 μs after the start of the pulse, and the detector is inactive and no longer biased after 18.03 μs having completed a full detector measurement pulse. The cycle then switches to another detector row ($N+1$). The PID setpoint has been marked by the horizontal line. The heater switch-off point is marked by a star while the TES state measurement for PID calculations is marked by a diamond.

Each detector is read out and maintained by a dedicated PID calculation

$$u(t) = K_P e(t) + K_I \int_0^t e(t')\mathrm{d}t' + K_D \frac{d}{dt} e(t) \ \text{[a.d.u]}, \tag{3}$$

where $u(t)$ is the output signal from the PID calculation and $e(t)$ represents an error signal from the desired state or setpoint. The proportional, integral, and derivative terms of Eq. (3) all have an associated gain or weighting factor, K_P, K_I, and K_D, respectively. The PID setpoint, which represents the desired operational state on the superconducting transition of a given detector, and associated gains can be adjusted on a per-detector basis (i.e., each detector has dedicated PID control).

As demonstrated in Fig. 4, the pulsed TDM operation typically involves bringing the TES state out of superconductivity through/past the setpoint and then allowing the TES state to relax through the setpoint back down to superconductivity. The PID controller modulates the heater power such that the TES state reaches the desired setpoint at the user-selected read index.

1.4 Detector Performance

We simulated the operation of a single feedback-controlled TES detector operating in this pulsed multiplexing scheme in LabVIEW software. These results are shown in Fig. 5 for a TES detector with a heat capacity of 0.4 nJ/K and an average thermal conductance of 4.0 μW/K. The TES in

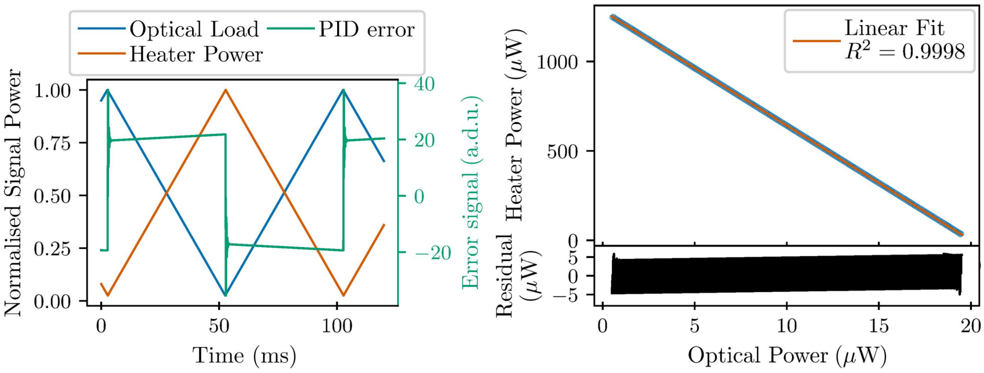

Fig. 5 Simulated response of a feedback-controlled TES and the PID error signal to a ramping optical signal (left). The linearity of the response of the detector signal (heater power) is also shown (right).

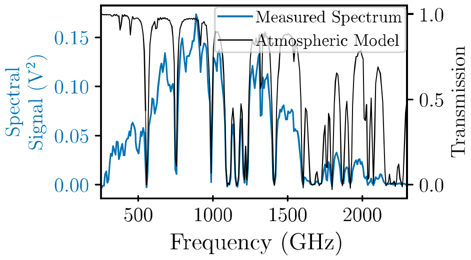

Fig. 6 Example spectral measurement made by the central detector of the TES array in the DFI testbed while viewing a 1100 00B0C blackbody source in raw detector units. An atmospheric model representative of the laboratory environment is also shown in black.

the simulation was set to transition at 9 K, following a sigmoidal curve to its normal-state resistance (200 data units) over 10 mK, and has been coupled to a 4 K thermal bath in the model. Under PID control set to the midpoint on the transition and operating with a 1/3 heater duty cycle, the TES detector responds well to the ramped optical signal and has excellent linearity to within 5 μW (~1.4% at expected optical loads). We have also simulated these results at different biases on the superconducting transition and a variety of transition slopes following values that can reasonably be fabricated, all showing similar performance.

Figure 6 shows a spectral measurement from the central detector of the TES array made with the DFI while viewing a heated blackbody source (see Benson[22]). A model spectrum from the open-air environment of the DFI optics was simulated using the atmospheric modeling software *am*[23] for comparison. The results shown in Fig. 6 demonstrate that TES detectors operating through PID feedback and with this multiplexing arrangement are capable of spectral measurements within the DFI testbed. Measurements of the heater power and the TES state, both operating under a constant-current bias, are made through voltage measurement with an analog-to-digital converter. The raw detector signal, being the heater power, is presented in units of squared volts (being proportional to optical power), and the TES temperature is represented in units of volts (assuming an ohmic device). We give a complete discussion of the optical performance and calibration of the detector array to optical units in Benson et al.[15] and Benson,[22] whereas in this work, we focus on improvements to raw detector performance through the tuning of user-adjustable parameters.

2 Detector Optimization

The QMC TES array was initially provided a set of general operational parameter settings by the manufacturer to achieve stable detector operation observing optical signals modulated up to 1 kHz with the intention of improving upon these for operation in the DFI instrument once it has been integrated into the optical assembly. We have performed investigations of the detector array's thermal behavior, noise performance, and response speed to determine a set of better-optimized parameters for measuring the interference signals from the DFI.

2.1 Thermal Characterization

The sensitivity of the PID feedback for a detector is increased by choosing a setpoint that occurs on the steepest part of the transitions (i.e., where α is at its maximum). As such, we expect that choosing the PID setpoint accordingly will improve detector performance. We measured the superconducting transitions of the detectors in situ by monitoring the TES voltage, where the cryostat was allowed to warm to a point at which all detectors had passed through their transitions. As these measurements were made *in situ*, the measured voltage includes impedance from the lines as in Fig. 4. A mirror was placed at the input to the detector cryostat effectively reducing the optical loading on the detectors (i.e., the detectors see themselves at ~8 K with minimal emission from the reflective room-temperature mirror; the mirror being thermally stable in the laboratory environment for timescales much longer than the time required for the TESs to transition). The temperature of the cryostat environment was monitored using a diode thermometer located on the detector block. These transitions are shown for the entire detector array in

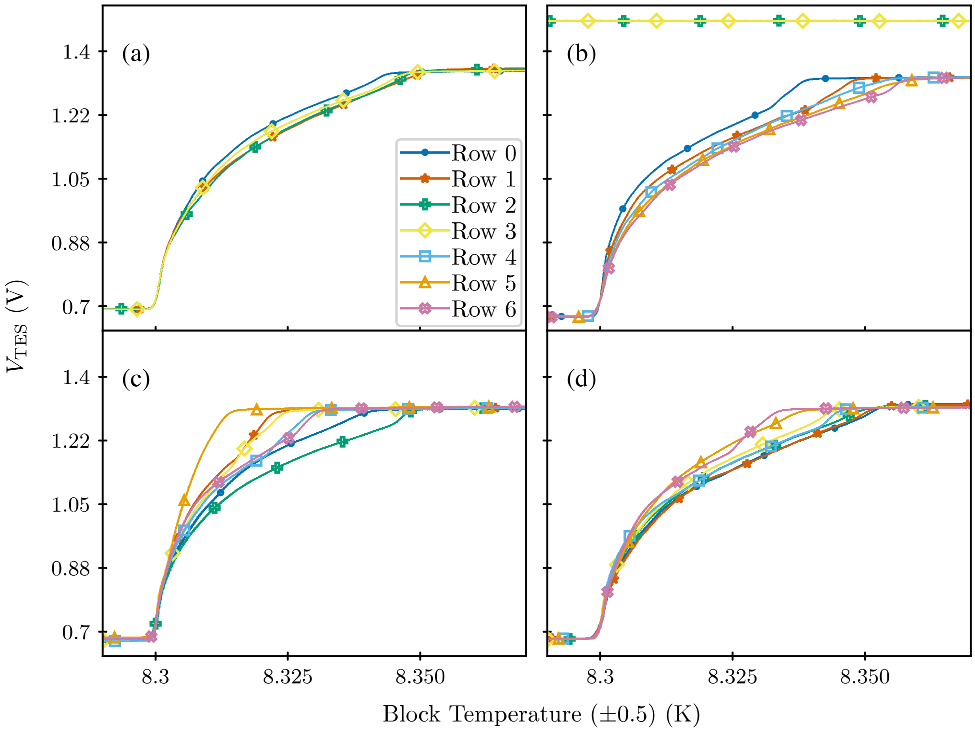

Fig. 7 Superconducting transitions of each active detector in the array separated by a multiplexing channel. Each curve is finely sampled, marked by the line. To help distinguish between each row in the multiplexing process, a large marker has been placed on each curve at a large interval and different colors are used. That is, the large markers do not show the actual sampling of these data.

Fig. 7. The calibration of the diode thermometer is such that there was a ±0.5 K uncertainty in the absolute temperature of the cryostat environment. The statistical uncertainty in temperature measurements was estimated to be ±30 mK from repeated measurements while the cryostat warmed from $\tilde{6}$ to ∼11 K.

As each TES operates under a constant current bias, α can be measured through the derivative of the TES voltage measurements of the superconducting transition [see Eq. (1)]. Due to noise in measurements of the TES state (having a 2.8-mV standard deviation), the derivative of the superconducting transition was determined from a smoothed spline fit to the curve. This is shown for the central detector in the left panel of Fig. 8 showing a maximum value $\alpha = 687 \pm 5$ at a TES voltage of ∼0.722 V. Maximum α values range from 565 to 1305 across the detector array with occurring at a TES bias of 0.722 to 0.752 V.

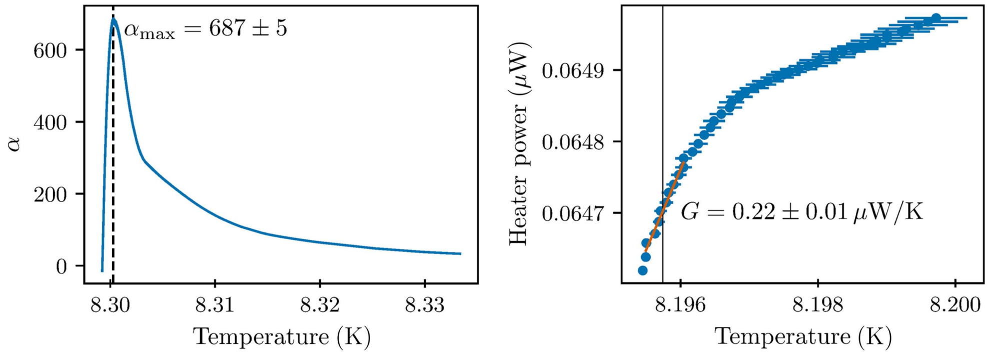

Fig. 8 Steepness of the superconducting transition of the central detector determined from a cubic spline fit of the measured curve is shown in the left panel. The right panel demonstrates the dynamic thermal conductance determined for the central detector.

Throughout these measurements, we noted that operating the detector array without multiplexing showed a much steeper transition than when measured in standard multiplexing mode. We attribute this to the self-heating of the detectors from the bias circuitry resulting in poor thermalization between an individual detector and the detector block (see Benson[22]). We note that the superconducting transition of the central detector that we measured and presented in Spencer et al.[24] did suffer from self-heating. The results presented here provide a more accurate measurement. Though we have not been able to provide a full thermal characterization of the detectors through *in situ* measurements with our current test equipment, we have obtained a measurement of the dynamic thermal conductance, $G = dP/dT$, for each detector. We have employed a technique similar to Karwan et al.[25] in which a small change in heater power and the corresponding change in TES temperature is monitored. In this way, G is measured directly as $G = \Delta P_{\text{heat}}/\Delta T$. For our system, the change in detector temperature is controlled by changing the setpoint of the PID and the heater power required to maintain the setpoint is monitored.

For the detector to maintain a set temperature in the steady state, it is required that Eq. (2) holds for input and output sources of thermal power in a sufficiently long time average. Provided that the time average of optical loading and electrical bias is constant, the change in the power-loading of the detector is given by $\Delta P = \Delta P_{\text{heat,avg}}$. Because the heater is only active for the specified duty cycle, whereas conduction occurs continuously, $G = 0.4\Delta P_{\text{heat}}/\Delta T$ for a detector operating with a pulse width of 10 loop counts, a blanking time of four loop counts, and without multiplexing.

Figure 8 shows thermal conduction measurements for the central detector. During this measurement, the heaters corresponding to each of the other detectors have been manually switched off and the detectors are not multiplexed to avoid deleterious thermal and electrical cross-talk.[22] To minimize changes in the optical load throughout measurements, a mirror was placed at the cryostat window. In the more sensitive lower region of the transition, the dynamic thermal conduction of the central detector remains at a constant value of 0.22 ± 0.01 μW/K. We found the repeatability in measurements of the superconducting transition to be the dominant source of uncertainty in our conduction measurements (see also Benson[22]).

Successful detector operation requires that the thermal conduction of a detector to the surrounding environment exceeds self-heating from the detector bias current so that a reduction in heater power (in response to an increase in optical load) can maintain a bias on the superconducting transition. This balance has been tuned with the current supply to the TES such that we have achieved successful operation with TES setpoints ranging the full transition.

2.2 Detector Timing

To characterize detector performance as a consequence of changes to the multiplexed measurement timing process, a mirror was again used to cover the detector window. Figure 9 demonstrates these measurements for the selection of heater activity times and TES state read delays. In general, we have found that if the heater activity time is too short (i.e., the dark purple curves in Fig. 9), the detector has poor performance and in many cases can be unstable. A heater activity time that becomes too great results in an increase in high-frequency noise. When the delay between the heater switch-off and TES state read (i.e., the “spacing” between these two parameters) is sufficiently small, measurements of the TES state occur on the rising edge of the TES state profile as the TES heats up. When a small spacing is coupled with a short heater time (purple curve in the upper left panel), a substantial amount of power is required to reach the setpoint often pushing the TES fully through its transition even after the PID measurement is made. Increasing the spacing between the heater switch-off and read index such that the TES state is measured for the PID on the falling edge (i.e., as the TES cools down through its transition) results in the narrowest distribution of detector signal. In addition, this results in low noise and a relatively flat white-noise level with a reasonable signal band. A spacing that is too large (i.e., the bottom row of Fig. 9) results in increased detector noise in general. In addition, these show deviations from a Gaussian distribution. As these timing settings are not suitable for low-noise measurements with the detector array, they are not further examined in this work. Further discussion on non-Gaussian noise in the system’s detector signal is discussed in Benson.[22]

To provide a rapid estimate of optimal detector performance in the parameter space, the distribution of the detector output signal while viewing a static optical load was fit with a

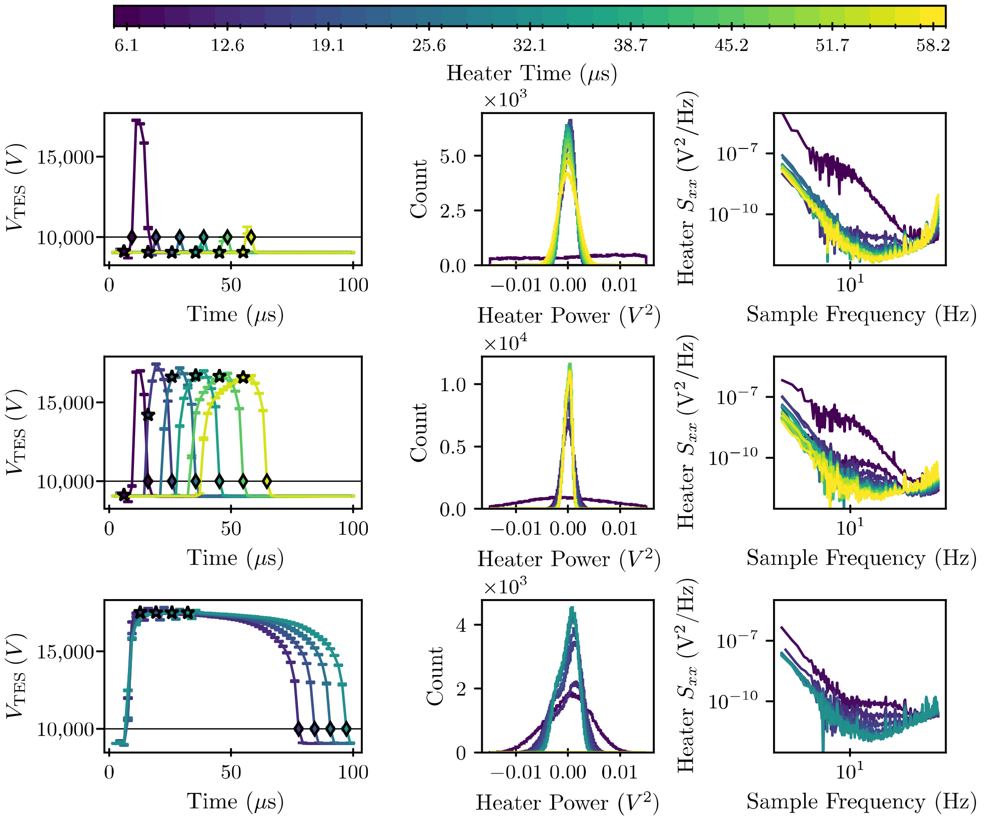

Fig. 9 Central detector performance for a selection of timing parameters while viewing a static optical load. The left column demonstrates the detector state throughout a single detector measurement pulse. The curves shown are the average profile of thousands of measurement pulses with varying heater activity times. The distribution of heater power values calculated by the PID loop is shown for each of these cases in the center column as is their respective noise power spectra in the right column. The chosen timing parameters show delays between the heater switch-off and TES state read that are two (top), six (middle), and 40 (bottom) loop counts (3.3, 9.9, and 66 μs, respectively). The heater switch-off and TES read index are marked in the TES state pulses as in Fig. 4 for each measurement curve. The longest heater durations are not shown for the bottom row as this would require increasing the detector measurement pulse width thereby changing the detector activity duty cycle relative to the other measurements.

Gaussian function to approximate broadband noise, shown in Fig. 10. Uncertainty in the fitted Gaussian width provides a measure of how well matched the noise profile is to a Gaussian distribution (shown by the error bars in Fig. 10). These measurements show that there are substantial improvements to performance by increasing heater activity time greater up six loop counts. For these heater activity times, a spacing of five to six loop counts between the heater switch-off and TES read index provides the best performance by these metrics.

Because the goal of the detector system is to measure optical modulation from the DFI (see Sec. 2.4), we have also studied the effects of changes to the timing of the detector measurements on the effective time constant of the central detector. A Toptica TERASCAN 1550 continuous wave photomixer was used as a THz source with a mechanical chopper to measure the response of the detectors to modulation up to ~1 kHz.[26] These results are shown in Fig. 11. Increasing the time that the heater remains active results in a change in the power required to maintain the PID feedback causing a natural offset in the response curves shown in Fig. 11. Increasing the total time required to measure a detector allows for greater durations of heater activity and longer TES state read delays to be accommodated resulting in a slower detector response. This is expected as increasing the total measurement time also increases the time required to complete an iteration of the PID process. To accommodate full Nyquist sampling of measurements over the full spectral

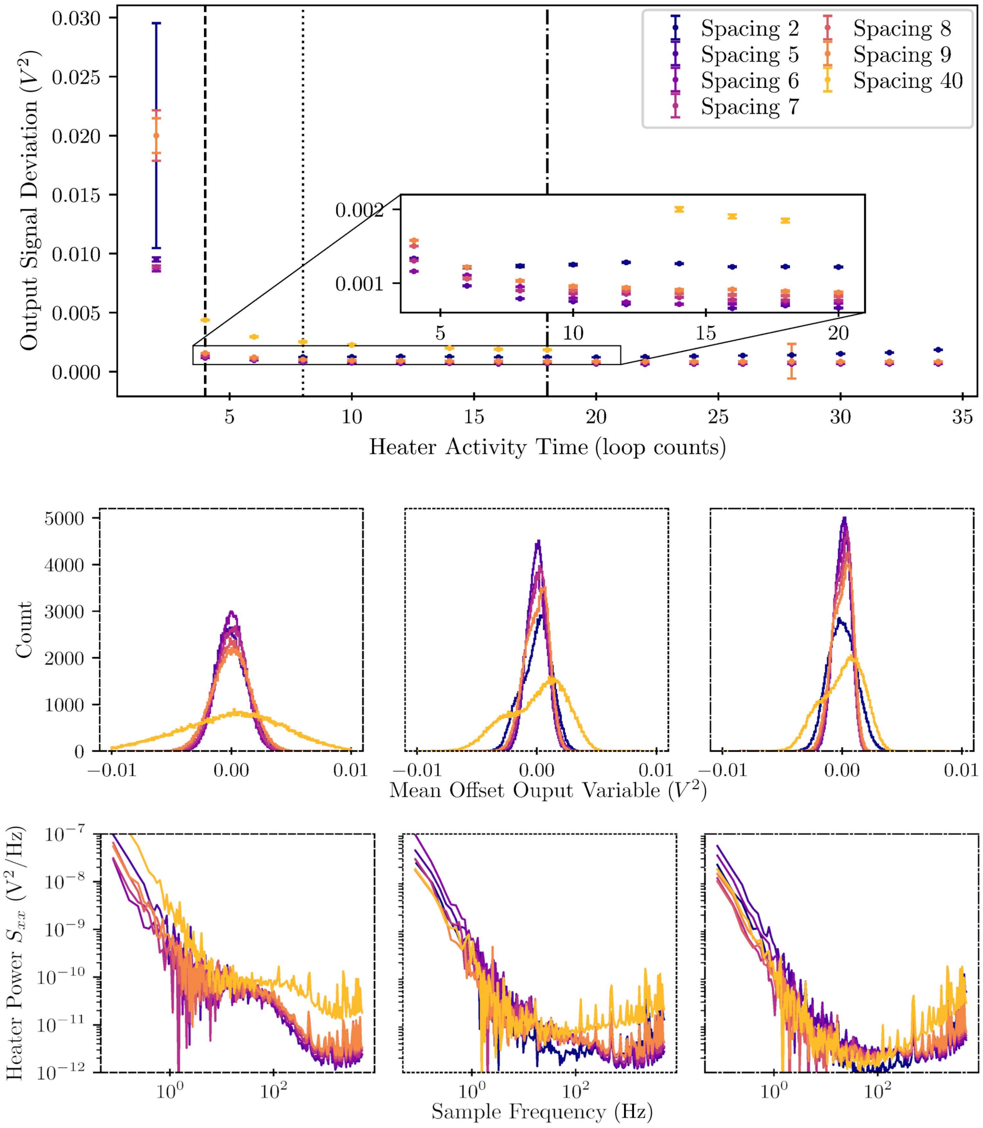

Fig. 10 Detector signal distribution widths for various blanking times and spacings (in loop counts) between the heater switch-off and the TES read index are shown in the top panel. Detector signal distributions at three selected blanking times (denoted by vertical lines at blanking times of 4, 8, and 18 in the upper panel) are also shown in the center row and the respective noise power spectral densities are shown in the final row.

band of the DFI, a total detector measurement time of less than 12.9 μs (12 loop counts) is needed. With this total measurement time, a heater activity time of 6.4 μs (six loop counts) and a TES read delay of 11.8 μs (11 loop counts) can be accommodated to reduce detector noise.

2.3 PID Tuning

Improper PID tuning can result in a variety of fail states in which a detector is unable to stabilize to a particular bias on the superconducting transition. The detector then oscillates between superconducting and normal conducting states. This often occurs when the action on the error signal in the PID loop is weighted too heavily causing the PID to consistently overshoot or undershoot the setpoint. Because the TES is not an effective temperature sensor either above or below its transition, it is possible for a detector to continue heating or cooling its thermal state without any change to the error signal in the PID when operating in temperature regimes outside of the transition.

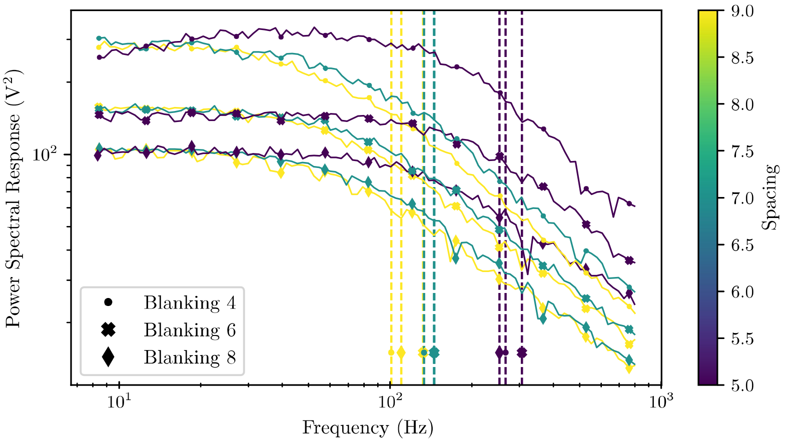

Fig. 11 Frequency response of the central detector operating with a variety of detector timing parameters. The dashed vertical lines indicate the −3 dB frequency cutoff of each response curve. The color shows the number of loop counts between the heater switch-off and the read index (spacing), whereas different markers indicate the blanking time. Each measurement was made with a pulse width set to be one greater than the read index such that the read index is the last loop count of a measurement pulse.

Provided the detector is properly stabilized, both the response speed and noise properties of each detector can be optimized for use with the DFI through further PID tuning. These effects are shown for the central detector while viewing a blackbody source chopped at 30 Hz placed in front of the detector window. The signal is averaged over several thousand periods of the chopped source in Fig. 12. It is evident that over this parameter range, increasing the proportional-term (P-gain) has a slight effect on the amplitude decreasing by 5.8% at the highest P-gain of 3000 data units. In addition, the integral gain (I-gain) has a dramatic effect on the ability of the detector to respond to optical modulation with a gain of 100 data units being near the limit of sufficient response at 30 Hz. Varying the derivative gain appears to have little effect on the output signal in the observed cases. These coupled with further measurements of a static optical load, suggest that the inclusion of the derivative term of the PID loop degrades detector performance.

To estimate the signal-to-noise ratio (SNR) of the detector, we measured the effects of P- and I-term weighting the PID feedback of the central detector while viewing a 90 °C blackbody modulated by a chopper at 40 Hz. Figure 13 demonstrates these results for a range of P- and I-term gains. The SNR of the detector with respect to broadband detector noise has been estimated by comparing the amplitude of the average chopped profile from several hundred periods of the chopper to the residual of the average profile on a per-chopper period basis. Detector SNR from this metric is shown in the left panel of Fig. 13. These coupled with the noise measurements

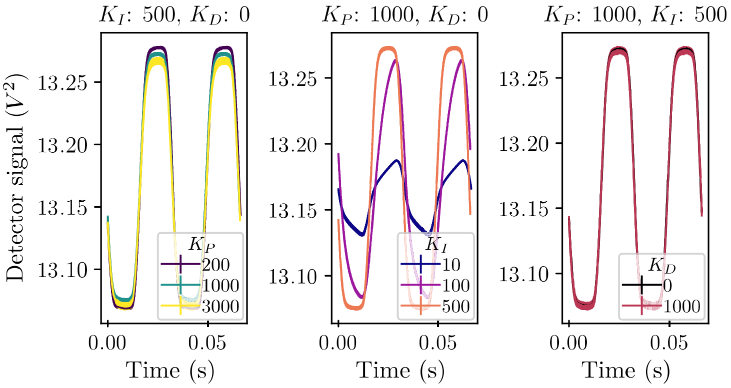

Fig. 12 Average central detector output signal while viewing a chopped blackbody source under a variety of PID conditions.

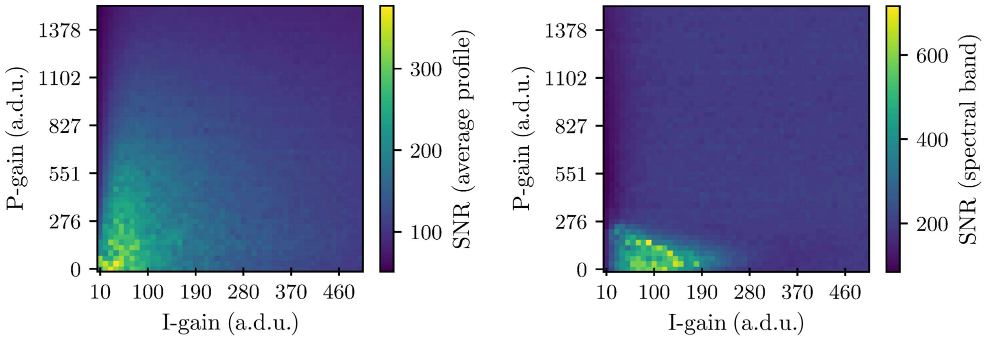

Fig. 13 Effect of varying proportional and integral-term gains on the SNR of central detector measurements of a 90 °C blackbody source chopped at 40 Hz. The left panel shows SNR measurements that compare the amplitude of the average chopped signal profile to noise measured in the full detector frequency band (average profile SNR). The right panel demonstrates similar measurements in which SNR has been estimated comparing the spectral peak corresponding to the modulated optical load to noise within the same frequency band (spectral band SNR).

of a static optical load suggest that broadband noise is reduced at low *P*- and *I*-term gains as the detector is less responsive to high-frequency noise. This represents a factor of ∼3 improvement in broadband SNR over the PID parameters that were set for the detector array without considerations for the DFI.

We expect broad-banded noise measurements shown in the left panel of Fig. 13 to be biased by the changing detector time constant (effectively rejecting more high-frequency noise with a lower time constant, see Fig. 14). To estimate the SNR of the central detector in a frequency band local to the chopped signal from the blackbody, we considered the power spectral density of the detector timeline over the peak modulation frequency with and without the chopped source. These measurements are shown in the right panel of Fig. 13. There is a localized range of *P*- and *I*-term gains for which the SNR in a frequency regime local to the signal from the chopped blackbody is improved by a factor of ∼2.6 over the initial parameters determined without considerations for the DFI.

Figure 12 has demonstrated that PID tuning can have a dramatic effect on the response of a detector and that the weight of the *I*-term plays a dominant role in this. To study the effects of PID tuning on detector response, we have measured the central detector response under a variety of PID conditions. Figure 14 shows a summary of *P*-term and *I*-term tuning on the effective time constant of the central detector. We have obtained these through a least-squares fit following the form of Eq. (1) to the detector's response while viewing the photomixer source with a chopper.

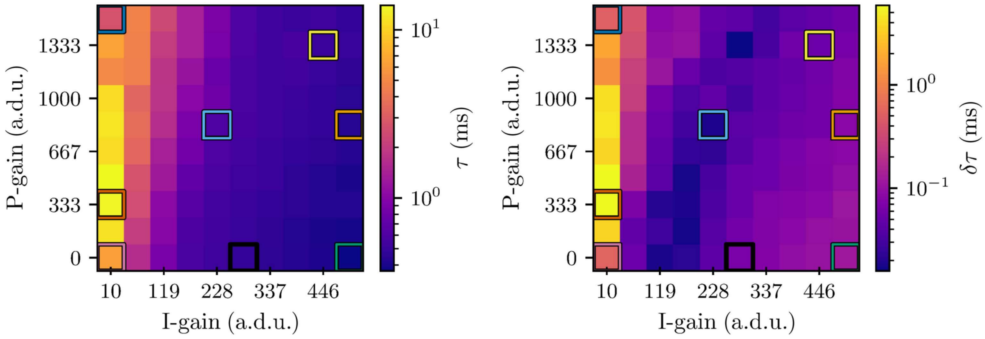

Fig. 14 Effective time constant (upper-left) and associated uncertainty (upper-right) of the central detector under different P and I term weighting in its PID control. Each time constant value is determined from a least-squares fit to the response of the detector to a photomixer source that has been modulated with a chopper wheel. Example cases that demonstrate irregular detector response profiles and examples of more typical behavior are outlined by a colored square. Their response profiles are shown in Fig. 15.

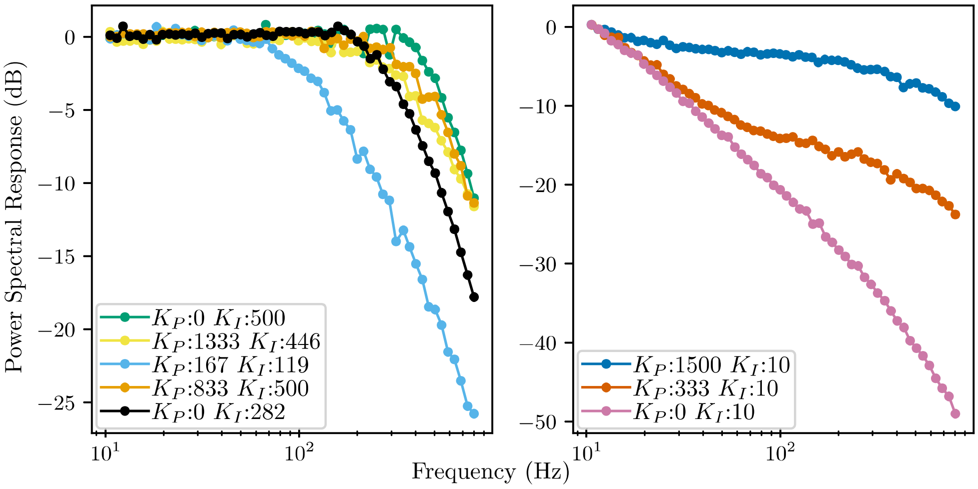

Fig. 15 Response of the central detector corresponding to particular *P* and *I* gain conditions of interest denoted in Fig. 14. Response measurements with an *I* gain of 10 (right panel) show nonlinear behavior prior to the high-frequency cutoff. These are shown in the right panel, whereas more typical responses are shown in the left.

These demonstrate that detector response speed is improved by a high weighting of the *I* term coupled with a low weighting of the *P* term.

In all cases explored, an I-term gain of 10 data units results in high uncertainty in the fitted detector time constant, as the PID control of the detector results in deviations from the response profile of a more typical bolometer (shown in the right panel of Fig. 15) despite good PID stability under these settings, e.g., the error signal stabilizes to random variations to within 1% between optical chops at 30 Hz for $K_P = 200K_I = 200$. These PID settings, which would introduce broad spectral artifacts, are not suitable for measuring the broad spectral band encoded in DFI interferograms. The error in the fitted time constant also provides a useful goodness-of-fit metric having a good correlation with suitable values of χ^2_{red}.

2.4 Low-Frequency Detector Noise

A DFI instrument produces time-varying interference signals that encode the spatial and spectral information of a source. The fastest varying modulation of light is a consequence of spectral interference and follows that of a standard FTS.[27–29] Thus, in spectral measurements of the DFI, the measured optical modulation can be chosen to occur over a signal band for which the detectors experience less noise by choosing an appropriate speed of travel for the moving mirror. We have found that the detectors in the array experience a significant $1/f$ noise (see Figs. 9 and 10). For the useful range of detector parameter settings, the modulation signal from the DFI should be kept above ∼7 Hz to avoid the $1/f$ dominated signal bands in all detectors.

We have demonstrated that modifications to the PID and measurement timing parameters of a detector can tune its noise performance (and thereby its SNR) and its response speed. Some trade-offs between these must be considered particularly for the choice of the integral term gain in the PID feedback. The specific requirements for detector response speed are governed by the spectral band-pass of the DFI. In Benson,[15] we measured the optical band of the DFI as 250 to 2200 GHz. Thus, the moving stage of the interferometer must be scanned at least as fast as 3 mm of optical path per second is required to avoid $1/f$-dominated signal bands at the lowest spectral band of the DFI. In addition, the detector time constants need only be as fast as 3.6 ms to fully Nyquist sample the spectral bandpass of the interferometer at this minimum scanning speed.

2.5 Spectral Noise

Balancing the detector time constant requirements for the interferometer operating in the spectral band and improvements to detector noise performance, we have determined a set of better-optimized detector parameters to reduce the noise in spectral measurements of the DFI made with the central detector of the array (see Table 1). Note that we have been conservative in our

Table 1 Detector parameters that we have determined to provide a better-optimized central detector for the DFI testbed are shown with the initial parameters. Selected detector performance metrics are also shown.

Detector parameter	Initial	Optimized
Pulse width (loop counts)	10	12
Blanking time (loop counts)	4	6
Read index (loop counts)	9	11
Setpoint (a.d.u.)	10,000	9500
P-gain (a.d.u.)	1000	600
I-gain (a.d.u.])	200	150
D-Gain (a.d.u.)	0	0
Detector time constant (ms)	0.96 ± 0.06	1.65 ± 0.01
Detector array framerate (kHz)	12.913	11.106

time constant selection to ensure that the time constant is fast enough to approximately twice-Nquist sample the modulation signal.

The spectral NEP of the DFI can be expressed using the expression for a nominal FTS

$$\mathrm{NEP_{FTS}} = \varsigma\sqrt{\frac{\Delta\sigma}{2v_{\mathrm{stage}}}}\ [\mathrm{W}/\sqrt{\mathrm{Hz}}], \tag{4}$$

where ς $[\mathrm{W/cm^{-1}}]$ represents spectral noise, v_{stage} [cm/s] is the scanning speed of the double-rooftop mirrors of the DFI (in units of optical path difference), and $\Delta\sigma$ $[\mathrm{cm^{-1}}]$ is the spectral resolution.[30,31] To determine spectral noise, we have considered 200 spectral scans of the DFI and subtracted the average spectrum from each single-scan spectrum. Assuming that the noise amplitudes of each scan are statistically independent, the total spectral noise is determined from the quadrature sum of the noise from each scan ($\varsigma^2 = 1/N^2 \sum_i^N \varsigma_i^2$). Figure 16 compares spectral noise in the central detector obtained from spectral measurements (in units of raw detector signal) of a blackbody source at 1100 °C using the initial detector parameters set by QMC Instruments and measurements using the optimized parameters. The corresponding $\mathrm{NEP_{FTS}}$ from each spectral noise measurement is also shown. For details on the spectral calibration of the DFI, see Benson et al.[15] and Benson.[22] The optimized detector parameters result in a 37% to 75% reduction in noise throughout the spectral band of the DFI (i.e., improving spectral noise by a factor of 1.6 to 4.8).

3 Conclusions and Future Work

The PID feedback-controlled array of TES bolometers that we have studied is a versatile system that can be optimized through the tuning of its PID feedback loops and adjusting the timing of its multiplexing process. Through *in situ* measurements of the superconducting transitions of the detector array, we have determined the optimal operational setpoints for the PID feedback of each detector. In addition, we have measured the dynamic thermal conductance of the central detector to be 0.22 ± 0.01 $\mu\mathrm{W/K}$ when operating about its optimal setpoint.

By modifying the timing of the multiplexing process and the PID tuning of the central detector, we have better optimized the central detector for use in the DFI testbed. This optimization requires the noise performance of the detector to be balanced with the speed required to effectively measure interference from the DFI. Our efforts have resulted in a 37% to 79% reduction in the noise of spectral measurements made with the DFI. This noise reduction can conceivably reduce the time required to achieve sufficient SNR in full spatial/spectral measurements from greater than 12 h to ∼6 to 8.

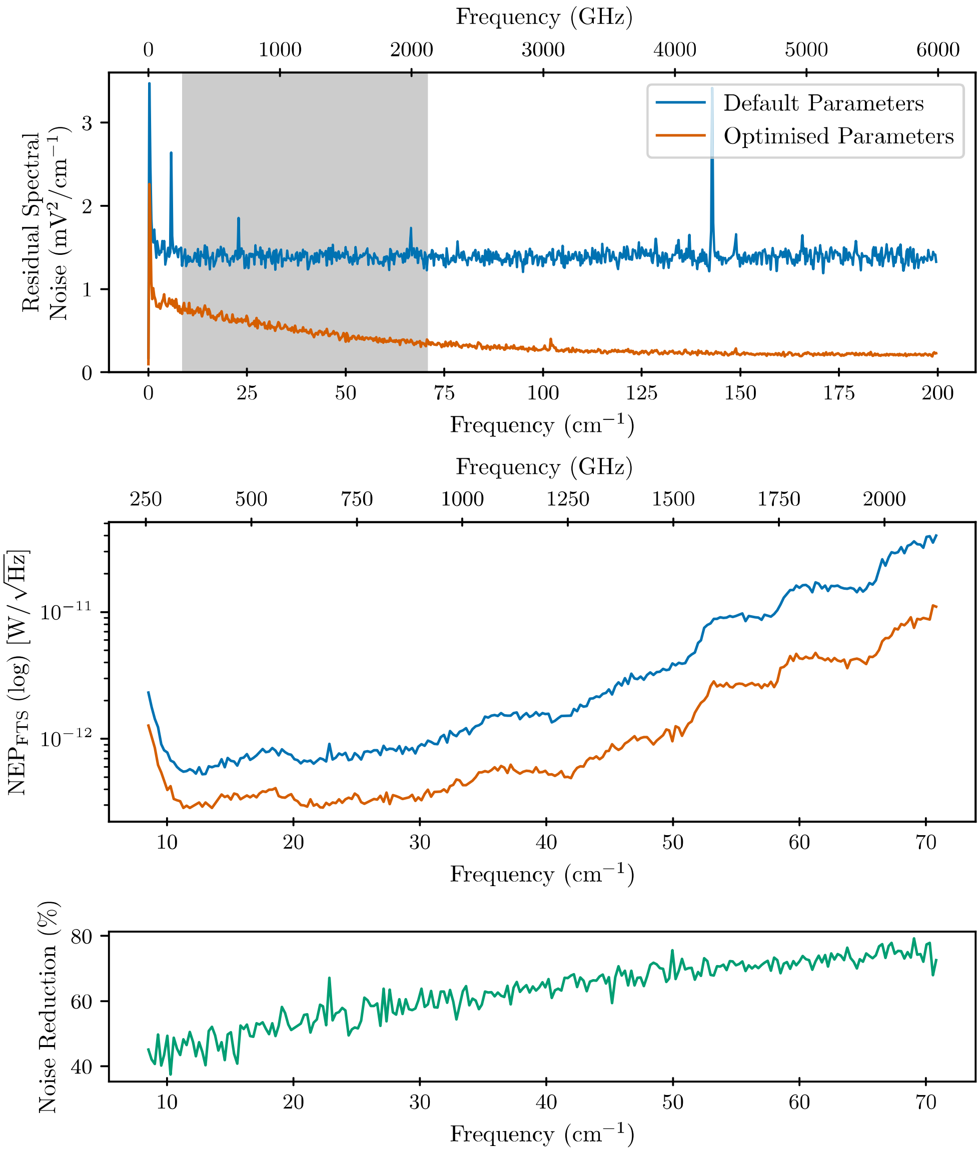

Fig. 16 Spectral noise of the central detector in the DFI testbed using initial and optimized detector parameters shown in uncalibrated units (top) and optical NEP (center). The region gray shaded region in the top panel marks the spectral bandpass of the DFI.

Although the focus of our efforts with the DFI testbed has been to demonstrate its capabilities as a spatial and spectral interferometer, the ultimate goal is to also leverage the wide-field capabilities of the DFI as an imaging spectrometer. In anticipation of this, the optimization of the full detector array should be investigated. Using the methodology and informed by the measurements presented here, we are extending the optimization process for the full array of 25 detectors.

Disclosures

The authors declare there are no financial interests, commercial affiliations, or other potential conflicts of interest that have influenced the objectivity of this research or the writing of this paper.

Code and Data Availability

The detector control software, code, and data in support of the findings do not have full public availability as they are entangled with the intellectual property of QMC Instruments. A subset of these are available from the authors upon request at BensonC@cardiff.ac.uk and with permission from QMC Instruments.

Acknowledgements

This development is supported by Canada Research Chairs (CRC), Canada Foundation for Innovation (CFI), Alberta Research Capacity Program (RCP), Alberta Innovates (AI), and Natural Science and Engineering Research Council of Canada (NSERC) grants and awards. We acknowledge CMC Microsystems and Canada's National Design Network (CNDN). We would like to acknowledge Mr. Vincent Weiler, Mr. Manimeldura Dinula De Silva, Mr. Himadri Saha, Mr. Klondike Taylor, and Ms. Yuxin Zhai for their contributions to laboratory infrastructure which made this work possible. In addition, we would like to acknowledge Dr. David Naylor and Blue Sky Spectroscopy for their contributions of vital test equipment to this research. We also thank the reviewers for their suggestions to improve the quality of this paper.

References

1. R. Hill, K. W. Masui, and D. Scott, "The spectrum of the universe," *Appl. Spectrosc.* **72**, 663–688 (2018).
2. F. P. Helmich and R. J. Ivison, "FIRI—a far-infrared interferometer," *Exp. Astron.* **23**, 245–276 (2009).
3. D. Farrah et al., "Review: far-infrared instrumentation and technological development for the next decade," *J. Astron. Telesc. Instrum. Syst.* **5**, 020901 (2019).
4. M. Harwit, D. Leisawitz, and S. Rinehart, "A far-infrared/submillimeter kilometer-baseline interferometer in space," *New Astron. Rev.* **50**(1), 228–234 (2006).
5. National Research Council et al., *Astronomy and Astrophysics in the New Millennium*, National Academies Press, Washington DC (2001).
6. D. Leisawitz et al., "The space infrared interferometric telescope (SPIRIT): high-resolution imaging and spectroscopy in the far-infrared," *Adv. Space Res.* **40**, 689–703 (2007).
7. A. Lyngvi et al., "Far infrared interferometer technology reference study," in *57th Int. Astronaut. Congr.*, p. A3–1 (2006).
8. G. Bignami and E. S. Agency, *Cosmic Vision: Space Science for Europe 2015–2025*, ESA Publications Division (2005).
9. D. Schito, S. Pezzuto, and W. Holland, "Far infra-red space interferometer critical assessment: definition/update of key science questions and relevant data products," Tech. Rep. Last editor: L. Spinoglio (2014).
10. H. Linz et al., "Bringing high spatial resolution to the far-infrared," *Exp. Astron.* **51**(3), 661–697 (2020).
11. D. T. Leisawitz et al., "Wide-field imaging interferometry testbed I: purpose, testbed design, data, and synthesis algorithms," *Proc. SPIE* **4852**, 255–267 (2003).
12. I. S. Ohta, M. Hattori, and H. Matsuo, "Development of a multi-Fourier-transform interferometer: imaging experiments in millimeter and submillimeter wave bands," *Appl. Opt.* **46**, 2881–2892 (2007).
13. R. Juanola-Parramon, *Far-Infrared Interferometer Instrument Simulator (FIInS)*, Springer International Publishing, Cham (2016).
14. J. Scott, C. Benson, and L. Spencer, "Design, operation, and characterization of a laboratory spatial-spectral Fourier transform interferometer," *IEEE Trans. Terahertz Sci. Technol.* **13**(6), 636–644 (2023).
15. C. S. Benson, J. P. Scott, and L. D. Spencer, "Detector performance and characterization in a double-Fourier interferometry testbed," in *Optica Sensing Congr. 2023 (AIS, FTS, HISE, Sensors, ES)*, p. JW2A.24, Optica Publishing Group (2023).
16. P. L. Richards, "Bolometers for infrared and millimeter waves," *J. Appl. Phys.* **76**, 1–24 (1994).
17. K. D. Irwin and G. C. Hilton, "Transition-edge sensors," in *Cryogenic Part. Detect.*, pp. 63–150 (2005).
18. P. D. Mauskopf, "Transition edge sensors and kinetic inductance detectors in astronomical instruments," *Publ. Astron. Soc. Pacif.* **130**, 082001 (2018).
19. M. K. Maul, M. W. Strandberg, and R. L. Kyhl, "Excess noise in superconducting bolometers," *Phys. Rev.* **182**, 522–525 (1969).
20. A. Gulian et al., "Current-biased transition-edge sensors based on re-entrant superconductors," *Phys. Procedia* **67**, 834–839 (2015).
21. M. Galeazzi, "An external electronic feedback system applied to a cryogenic-calorimeter," *Rev. Sci. Instrum.* **69**, 2017–2023 (1998).
22. C. S. Benson, "Feedback-controlled transition edge sensor bolometers in a far-infrared double-Fourier interferometer," PhD thesis, University of Lethbridge (2024).
23. S. Paine, *The am Atmospheric Model*, Smithsonian Astrophysical Observatory.
24. L. D. Spencer et al., "Optimization of a cryogenic transition-edge sensor detector array for far-infrared astrophysics," *Proc. SPIE* **12180**, 121802S (2022).
25. K. Rostem et al., "Thermal conductance measurements for the development of ultra low-noise transition-edge sensors with a new method for measuring the noise equivalent power," *Proc. SPIE* **7020**, 70200L (2008).

26. A. J. Deninger et al., "2.75 THz tuning with a triple-DFB laser system at 1550 nm and InGaAs photomixers," *J. Infrared Millim. Terahertz Waves* **36**, 269–277 (2015).
27. W. F. Grainger et al., "Demonstration of spectral and spatial interferometry at THz frequencies," *Appl. Opt.* **51**, 2202 (2012).
28. M. Born and E. Wolf, *Principles of Optics*, Cambridge University Press (2019).
29. L. D. Spencer et al., "A Fourier transform spectrometer for ground testing of the Herschel/SPIRE instrument," *Proc. SPIE* **5487**, 501–512 (2004).
30. L. D. Spencer, "Imaging Fourier transform spectroscopy from a space-based platform: the Herschel/SPIRE Fourier transform spectrometer," PhD thesis, University of Lethbridge (2009).
31. E. Serabyn and E. W. Weisstein, "Fourier transform spectroscopy of the Orion molecular cloud core," *Astrophys. J.* **451**, 238 (1995).

Chris S. Benson is a research associate at Cardiff University. He received his BS (hons.), MSc, and PhD degrees in physics and experimental astrophysics from the University of Lethbridge, Canada, in 2018, 2020, and 2024, respectively. He has worked on Herschel SPIRE data calibration and is working on the South Pole Telescope Summer-time Line Intensity Mapping spectrometer/focal plane. His current research interests include Fourier transform spectroscopy, double-Fourier interferometry, mm-wave and terahertz detectors, and on-chip spectrometers.

Jeremy P. Scott is a research associate at the University of Arizona. He received his BSc, MSc, and PhD degrees in physics and astronomy from the University of Lethbridge, Canada, in 2014, 2017, and 2024, respectively. His research interests include double-Fourier interferometry, nulling interferometry, transition edge sensor bolometers, and modeling these systems. He is currently preparing the Nulling Observations of exoplaneTs and dusT instrument for its visit to the Very Large Telescope Interferometer.

Locke D. Spencer received his BSc degree in engineering physics from the University of Alberta, Edmonton, AB, Canada, in 2003 and his MSc degree in physics and his PhD from the University of Lethbridge, Lethbridge, AB, Canada, in 2005 and 2009, respectively. From 2009 to 2013, he was with the Cardiff University School of Physics and Astronomy, Cardiff, Wales, U.K. From 2013 to 2023, he was a Canada Research Chair (II) in experimental astrophysics. He is currently an associate professor with the University of Lethbridge specializing in instrumentation and data analysis for current and future far-Infrared astrophysics.

Rashmi V. Sudiwala is a senior research fellow at Cardiff University. He received his BS (hons.) and PhD degrees in physics from Queen Mary College, University of London, in 1983 and 1987, respectively. He has worked on a number of instruments including the Planck HFI, SCUBA2, and BICEP2 and is currently working on the Simons Observatory UK receivers.

Biographies of the other authors are not available.